Original Article

Visualization and quantification of *de novo* lipogenesis using a *FASN-2A*-GLuc mouse model

Wenjiao Li[1], Song Zhang[1,2], Xin Fu[1], Jiehao Zhang[1], Renlong Li[1], Haohao Zhang[1], Qingling An[3], Weizhen Wang[1], Zuhong Tian[1], Changhong Shi[3], Yongzhan Nie[1]

[1]State Key Laboratory of Cancer Biology, National Clinical Research Center for Digestive Diseases and Xijing Hospital of Digestive Diseases, Air Force Medical University of PLA, Xi'an, China; [2]Department of Gastroenterology, General Hospital of Central Theater Command, Wuhan, China; [3]Laboratory Animal Center, Air Force Medical University of PLA, Xi'an, China

Contributions: (I) Conception and design: W Li, Y Nie; (II) Administrative support: Y Nie; (III) Provision of study materials: W Li, S Zhang, X Fu, J Zhang, R Li, H Zhang, C Shi; (IV) Collection and assembly of data: W Li, S Zhang, X Fu, W Wang; (V) Data analysis and interpretation: Q An, Z Tian; (VI) Manuscript writing: All authors; (VII) Final approval of manuscript: All authors.

Correspondence to: Yongzhan Nie. Xijing Hospital of Digestive Diseases, 127 West Changle Rd, Xi'an 710032, China. Email: yongznie@fmmu.edu.cn.

Background: De novo lipogenesis (DNL) is a dynamic process that converts excess carbohydrates into fatty acids to maintain cellular homeostasis. Dysregulation of DNL is associated with diverse obesity-related diseases and many tumor types. Therefore, monitoring DNL in real-time with high sensitivity should be highly beneficial when screening therapeutic agents for their potential use as obesity treatments.

Methods: A sequence coding for Gaussia luciferase (GLuc) preceded by a 2A peptide was inserted into the murine fatty acid synthase (FASN) genetic locus by homologous recombination to generate FASN-2A-GLuc mice. The luciferase mouse model was evaluated in conditions of physical and pharmacological stimuli by in vivo and ex vivo imaging.

Results: The distribution of bioluminescence signals in different organs was identical to the FASN expression: high in white fat, brown fat, and the lungs. In addition, the bioluminescence signals accurately recapitulated the dynamic change of FASN in response to fasting and refeeding conditions. Moreover, with this murine reporter model, we also discovered that fatostatin, a synthetic inhibitor of sterol regulatory element-binding proteins, effectively inhibited DNL in multiple organs, especially in adipose tissues under a high-carbohydrate diet.

Conclusions: Our FASN-2A-GLuc reporter mouse model proved to be a sensitive visualization tool for monitoring both systemic and organ-specific DNL in real time.

Keywords: Bioluminescence imaging (BLI); de novo lipogenesis (DNL); fatty acid synthase (FASN); fatostatin

Submitted Mar 03, 2022. Accepted for publication Jul 04, 2022.
doi: 10.21037/atm-22-1132
View this article at: https://dx.doi.org/10.21037/atm-22-1132

Introduction

De novo lipogenesis (DNL) provides cells with a continuous supply of lipids mainly derived from excess carbohydrates, which helps to protect against glucotoxicity while providing energy storage. DNL is catalyzed through a coordinated series of enzymatic reactions by ATP-citrate lyase, acetyl-CoA carboxylase, and fatty acid synthase (FASN; also known as FAS). FASN catalyzes palmitate biosynthesis by using acetyl-CoA and malonyl-CoA in an NADPH-dependent reaction, which generates the first endogenous lipid during DNL. As the rate-limiting enzyme of DNL, FASN is believed to play a decisive role in the maximal capacity of lipogenesis (1).

The DNL process is closely associated with nutritional status and hormones, which are more active in the liver

and adipose tissues. Most enzymes involved in DNL are primarily regulated at the transcriptional level through the activation of sterol regulatory element-binding proteins (SREBPs) and carbohydrate response element-binding protein (ChREBP) (2,3). Insulin promotes glucose absorption from the blood and induces the expression of SREBP (4). Glucose provides a carbon source for DNL via the glycolytic pathway, and glucose metabolites have the ability to activate ChREBP (5). Compared with carbohydrates, a high-fat diet inhibits DNL by blocking the activation of ChREBP (6). Leptin, a hormone produced primarily by adipocytes, suppresses the expression of the enzymes involved in the lipogenic pathway by decreasing SREBP-1 (7).

Aberrant DNL is associated with a variety of chronic diseases, including obesity, type 2 diabetes mellitus, nonalcoholic fatty liver disease (NAFLD), and numerous cancers (8-10). The most common cause of aberrant DNL is abnormal insulin signaling. Insulin resistance or insufficient insulin secretion decreases the use of glucose in extrahepatic tissues, which serves as a substrate for hepatic DNL independent of insulin signaling. Elevated DNL is a critical contributor to the development of NAFLD (11). Obesity affects DNL by elevating hepatic DNL and decreasing adipocyte DNL (12). Further, the beneficial lipid product of adipocyte DNL, palmitic acid esters of hydroxy fatty acids, decreases inflammation and enhances insulin-stimulated glucose uptake (13). In various types of cancer cells, DNL level is increased, which supports the abundance of energy substrates and enhances membrane biogenesis in rapidly proliferating cells (14). Hence, the modulation of DNL may be a potential therapeutic target for obesity-associated metabolic diseases. However, it remains unclear what degree of DNL inhibition is optimal for producing curative effects, and there are minor side effects to consider based on the variability among different tissues. Therefore, monitoring DNL systemically and organ-specifically is essential for studying the regulatory network and screening effective therapeutic agents.

Bioluminescence imaging (BLI) is a sensitive and noninvasive optical tool that has recently attracted substantial attention. BLI is based on a substrate-oxidation reaction catalyzed by luciferase that produces detectable light (15). Thus, BLI can be used to optically trace spatiotemporal gene expression dynamically by expressing different luciferase reporters in living cells and animals. Based on these advantages, BLI has been widely applied in the fields of tumor growth and metastasis, cellular apoptosis and tracking, bacterial and viral infections, and drug development (16-18). Previous data showed that BLI enabled systematic imaging of brown and brite fat recruitment in a murine model using an uncoupling protein 1 (UCP1)-based luciferase reporter (19). Another study used BLI to show the sequential *in vivo* induction of two key gluconeogenesis transcription factors with adenoviral CRE-luciferase and G6Pase-luciferase reporters (20). These studies provided excellent examples of monitoring dynamic energy metabolism in a more visual and real-time manner. However, no mouse model has been developed for dynamic and longitudinal monitoring of the endogenous DNL process.

In this study, we inserted the coding sequence of Gaussia luciferase (GLuc) into the murine *FASN* gene locus to monitor endogenous FASN expression *in vivo* and *ex vivo* using BLI. Our results showed that the organ-specific distribution of GLuc signals was consistent with FASN expression. When the nutritional status changed, the bioluminescence signal remained synchronized with *FASN* gene expression, decreasing significantly during the fasted station and rapidly recovering after refeeding. With this model, we found that fatostatin, an inhibitor of SREBPs, effectively inhibited DNL in multiple organs and decreased the food intake of mice. Overall, our FASN-2A-GLuc reporter mouse model faithfully enabled the detection of endogenous FASN expression in a dynamic, noninvasive, and systemic manner. We present the following article in accordance with the ARRIVE reporting checklist (available at https://atm.amegroups.com/article/view/10.21037/atm-22-1132/rc).

Methods

Generation of FASN-2A-GLuc

FASN-2A-luciferase reporter mice were generated by inserting the 2A-GLuc sequence between exon 43 of the endogenous *FASN* gene and its 3'-untranslated region (UTR). The left homologous arm was inserted 5.6 kb upstream of the stop codon of FASN, and the right arm was inserted 5.2 kb downstream of the 3'-UTR. An FRT-flanked neomycin-resistance cassette was inserted 246 bp downstream of the 3'-UTR. Embryonic stem cell clones were screened by Southern blotting using 5' and 3'probes. The neomycin-selection cassette was removed before the cells were used for producing chimeras. FASN-2A-GLuc mice were

identified by polymerase chain reaction (PCR)–based genotyping using the following primers: forward primer: 5'-GATGGGACCTCGGGTAATTTGG-3', reverse primer: 5'-GTCTTGCCTGTGATAGACCTTAG-3'.

Animal studies

All animal experiments conducted in this study were approved by the Institutional Animal Care and Use Committee (IACUC) of the Air Force Medical University of PLA in China (No. IACUC-20181204) and were performed in accordance with the Guide for the Care and Use of Laboratory Animals, 8th edition. C57BL/6J mice were housed in a pathogen-free animal facility at 22±2 ℃ under a controlled 12-h light-dark cycle. We performed the following studies with male litter FASN-2A-GLuc mice: (I) a fasting and refeeding study, in which mice were randomly split into 3 groups (n=5–6 mice/group)—the *ad libitum* feeding group, the fasting group (fasting for 24 h), and the refeeding group (fasting for 24 h and refeeding for 4 h); and (II) a fatostatin-administration study (n=5– 6 mice/group), in which mice were given glucose and fructose solutions (Sigma-Aldrich, St. Louis, MI, USA) and treated intraperitoneally with either corn oil (control) or fatostatin (30 mg/kg; Selleck Chemicals, Houston, TX, USA) daily for 6 days.

In vitro analysis of luciferase activities

Luciferase activities were measured in tissues and mouse serum samples with the Pierce Gaussia Luciferase Flash Assay Kit (Thermo Fisher Scientific, Waltham, MA, USA) using a Varioskan Flash multimode reader (Thermo Fisher Scientific). GLuc-containing serum or GLuc-negative serum (10 μL) samples were added directly to separate wells of a 96-well black microtiter plate (Corning, Inc., Corning, NY, USA). GLuc activity was detected by adding 50 μL of coelenterazine working solution (1 mg/mL) to each well and acquiring photon counts for 10 s, as previously described (21). Mouse tissues were homogenized for 20 s with lysis buffer and lysed for 30 min on ice. The tissue lysates were then centrifuged at 10,000 ×g for 15 min at 4 ℃, and 10 μL of each resulting supernatant was mixed with 50 μL of coelenterazine working solution in the wells of a 96-well black microtiter plate. GLuc activities were detected and normalized to the total protein concentration in each sample.

In vivo and ex vivo BLI analysis

BLI was performed with an *in vivo* imaging system (PerkinElmer, Waltham, MA, USA). Coelenterazine was first dissolved in methanol (5 mg/mL) and then diluted to 1 mg/mL in phosphate-buffered saline without calcium chloride or magnesium chloride. Before imaging, the fur covering the regions of interest was removed with a commercial electrical razor. For *in vivo* luciferase imaging, mice were injected intraperitoneally (i.p.) or intravenously (i.v.) with 5 mg/kg body weight of coelenterazine (Yeasen, Shanghai, China). The mice were anesthetized with 2.5–3.5% isoflurane in an anesthesia box for 5 min and then transferred to the imaging chamber. The mice were imaged continuously at 1-min intervals, with the total imaging time dependent on the experiment. All *in vivo* images were quantified with Living Image Software (PerkinElmer). For *ex vivo* imaging, freshly isolated organs and tissues were placed into 12-well culture plates containing chilled phosphate-buffered saline and subjected to BLI under the following settings: sensor-exposure time, 60 s; binning, 4; and speed index, 1.

Western blot analysis

Tissue samples (white fat, 100 mg; other tissues, 30 mg) were lysed with radioimmunoprecipitation assay buffer (4A Biotech Co., Ltd., Beijing, China) for 30 min on ice and centrifuged at 12,000 ×g for 15 min at 4 ℃. Protein samples were resolved on 4–20% sodium dodecyl sulfate-polyacrylamide gels (Beyotime Biotechnology, Shanghai, China) and electrotransferred onto nitrocellulose membranes (Merck Millipore, Burlington, MA, USA). The membranes were probed overnight with specific antibodies at 4 ℃, washed 3 times with Tris-buffered saline containing 0.05% Tween 20, and incubated with a horseradish peroxidase-conjugated anti-rabbit immunoglobin G (IgG) antibody for 1 h at room temperature. The membranes were developed with UltraSignal ECL reagent (4A Biotech Co., Ltd.). The protein expression levels were quantified with ImageJ software (National Institutes of Health, Bethesda, MD, USA) (22). Primary antibodies against FASN (1:1,000; Cell Signaling Technology, Danvers, MA, USA), GLuc (1:500; New England Biolabs, Ipswich, MA, USA), and β-tubulin (1:2,000; Proteintech, Wuhan, China) were used in the experiments.

RNA extraction, reverse transcription, and quantitative PCR analysis

Total RNA (500 ng) was isolated from tissues using the RNeasy Mini Kit (Qiagen, Hilden, Germany), and complementary DNA was generated with PrimeScript RT Master Mix (Takara Bio, Inc., Kusatsu, Japan). Gene expression levels were determined by real-time PCR using the QuantiTect SYBR Green PCR Kit (Roche, Basel, Switzerland) on a LightCycler 480 instrument II (Roche). All data were normalized to β-tubulin RNA expression.

Metabolic cage

Systemic energy metabolism in mice administered with fatostatin was continuously measured using the Comprehensive Lab Animal Monitoring System (Columbus Instruments, Columbus, OH, USA). Mice were weighed and individually housed in metabolic chambers. After their adaptation to the environment, the following parameters were monitored: oxygen consumption (VO_2), carbon dioxide production (VCO_2), respiratory exchange ratio (RER), heat, drink intake, food intake, and activity.

Statistical analysis

All data are expressed as the mean ± SEM. Statistical analyses were performed using GraphPad Prism 8 software (GraphPad Software, Inc., San Diego, CA, USA). A 1-way analysis of variance (ANOVA) was used to compare values obtained from 3 or more groups, which was followed by Tukey's post hoc test. The Student's *t* test was performed to compare values obtained from 2 groups. P values <0.05 were considered to reflect statistically significant differences.

Results

Generation and characterization of FASN-2A-GLuc mice

To generate luciferase reporter mice for endogenous FASN, we inserted the coding sequence for GLuc preceded by a 2A peptide-encoding sequence between the 3'-UTR and the last coding exon of the murine FASN gene by homologous recombination (*Figure 1A*). The 2A peptide functioned as a cis-acting hydrolase element to mediate a cleavage reaction between proteins, thus enabling the expression of flanking genes to be transcribed under a single open reading frame (23). We verified successful homologous recombination by PCR analysis and agarose gel electrophoresis. The corresponding PCR products of wild-type (WT) mice were 201 bp long, and those from FASN-2A-GLuc knock-in ($FASN^{+/GLuc}$) mice were 201 and 287 bp long (*Figure 1B*).

The protein expression levels of GLuc and GLuc-Fusion in liver tissues were detected by western blot analysis. The results showed that the GLuc protein was expressed in $FASN^{+/GLuc}$ mice but not in the negative control and WT mice. (*Figure 1C*). The GLuc enzyme is a relatively small, secreted, thermostable protein (24). Thus, we also detected the levels of GLuc in mouse sera, finding that it was present at approximately 100-fold higher levels in $FASN^{+/GLuc}$ mice than in WT mice (*Figure 1D*). We next assessed the luciferase activities by performing *in vivo* BLI (*Figure 1E*) and *ex vivo* BLI in epididymal white adipose tissue (eWAT), brown adipose tissue (BAT), the liver, the kidneys, and visceral WAT (vWAT) (*Figure 1F*). Consistent with the protein expression level of GLuc, the luciferase signal was only detected in $FASN^{+/GLuc}$ mice. Taken together, these results indicated that the FASN-2A-luciferase reporter mouse model was generated successfully.

In vivo kinetics of GLuc following i.v. and i.p. substrate administration

To ensure the optimal administration route and detection time for *in vivo* BLI, GLuc activity kinetics were determined after administering coelenterazine (a GLuc substrate) by either i.v. or i.p. injection. First, $FASN^{+/GLuc}$ mice were imaged continuously at 1-min intervals following coelenterazine injection into the caudal vein. We observed that the bioluminescence signals were significantly reduced within the first 5 min after substrate injection. After 30 min, the bioluminescence signal was reduced by over 90% compared to the initial value. Initially, the luciferase signals were distributed throughout the whole body but were later concentrated in the abdomen (*Figure 2A*). Thus, administration by i.v. suited experiments with a short assay time involving molecules that undergo rapid metabolism. The bioluminescence signal remained stable within the first 20 min, after which the signal gradually decreased over time when coelenterazine was i.p. injection. The luciferase signal was primarily distributed in the abdomen (*Figure 2B*). Importantly, administration by i.p. was simpler to perform and was more suitable for intergroup comparisons.

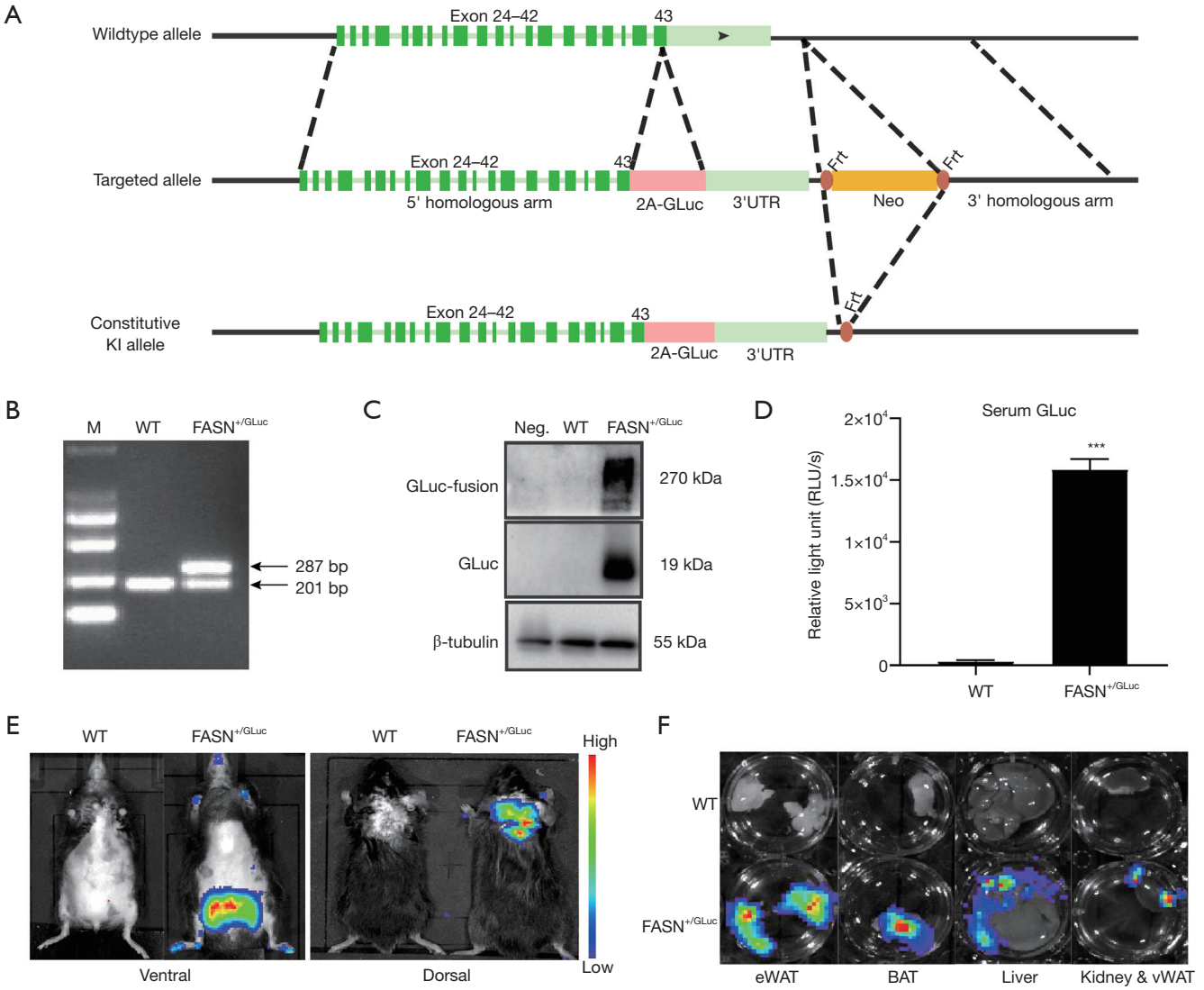

Figure 1 Generation and characterization of FASN-2A-GLuc mice. (A) A schematic illustration of the FASN-2A-GLuc knock-in strategy. (B) Genotyping-based identification of WT and FASN-2A-GLuc knock-in mouse (FASN$^{+/GLuc}$) by PCR. The DNA product of WT was only 201 bp, in which 2 PCR products were formed (201 and 287 bp) with FASN$^{+/GLuc}$ mice. (C) Protein expression levels of GLuc-fusion and GLuc in liver tissues were analyzed by western blotting. (D) GLuc activities in serum from WT and FASN$^{+/GLuc}$ mice. (E) *In vivo* luciferase imaging of WT and FASN$^{+/GLuc}$ mice. (F) *Ex vivo* luciferase imaging in freshly isolated eWATs, BATs, liver tissue, kidney tissues, and vWATs from WT and FASN$^{+/GLuc}$ mice. The data shown were analyzed by Student's *t* test. The graphs show mean values ± SEMs. ***, P<0.001. M, molecular size markers; Neg, negative control; GLuc, Gaussia luciferase; eWAT, epididymal white adipose tissue; BAT, brown adipose tissue; vWAT, visceral white adipose tissue.

Organ-specific GLuc bioluminescence in FASN-2A-GLuc mice

We monitored the bioluminescence of multiple organs *ex vivo* and compared the findings with the corresponding endogenous FASN expression levels. First, we ascertained *in situ* bioluminescence for FASN-2A-GLuc mice using BLI. The signals were concentrated in the eWAT in the supine position. In the scapula region, the signals were observed mainly in the BAT and subcutaneous WAT (*Figure 3A*). We then detected the bioluminescence in freshly isolated mouse organs by *ex vivo* imaging.

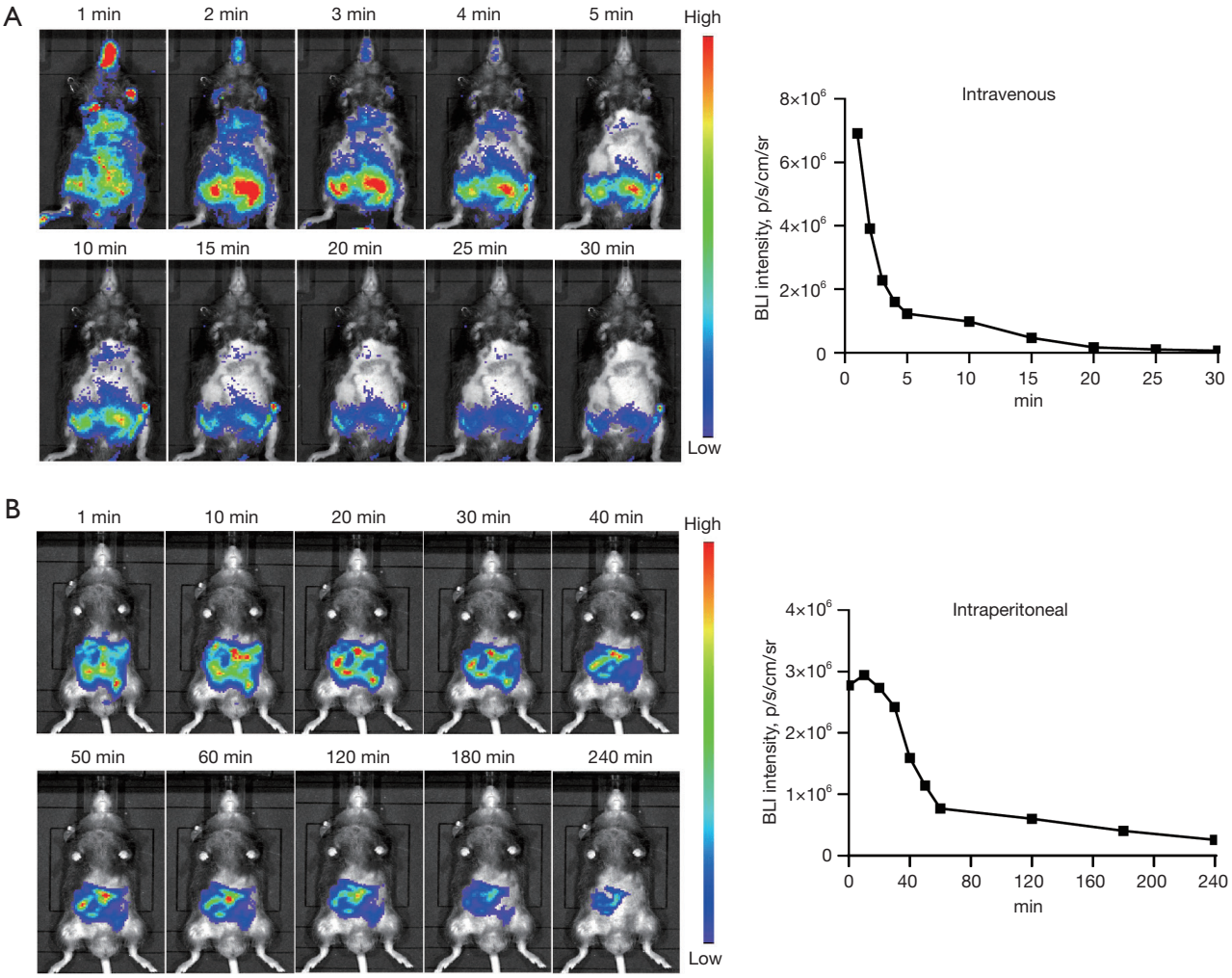

Figure 2 The kinetics of GLuc *in vivo* imaging. (A) Representative BLI (left) and quantification (right) after coelenterazine injection by i.v. (B) BLI (left) and quantification (right) after coelenterazine injection by i.p. The results shown are from 1 representative mouse from each group. Three independent experiments were performed with each group. GLuc, Gaussia luciferase; BLI, bioluminescence imaging; i.v., intravenously; i.p., intraperitoneally.

Quantitative analysis of the bioluminescence intensities showed that the signals were higher in the WAT, BAT, and lungs than in the liver, heart, and kidneys (*Figure 3B*). The GLuc activities in different tissue lysates were evaluated with a GLuc assay kit, and the results were consistent with those obtained by *ex vivo* imaging (*Figure 3C*). Finally, the messenger RNA (mRNA; *Figure 3D*) and protein (*Figure 3E*) levels of FASN were detected in these organs to study organ-specific bioluminescence intensities. The general trends of the FASN levels in different organs were consistent with the GLuc bioluminescence results.

Visualization of FASN expression patterns in FASN-2A-GLuc mice under ad libitum, fasted, and refed conditions

We evaluated bioluminescence changes after fasting and refeeding conditions to test whether the bioluminescence values varied along with changes in endogenous FASN expression. First, we observed the bioluminescence changes when mice fasted for 6 or 12 h. The bioluminescence tended to decrease after the mice had fasted for 6 h and significantly decreased after the mice had fasted for 12 h (*Figure 4A*,*4B*). Following this, the reporter mice were fasted for 24 h and refed for 4 h. The results showed that

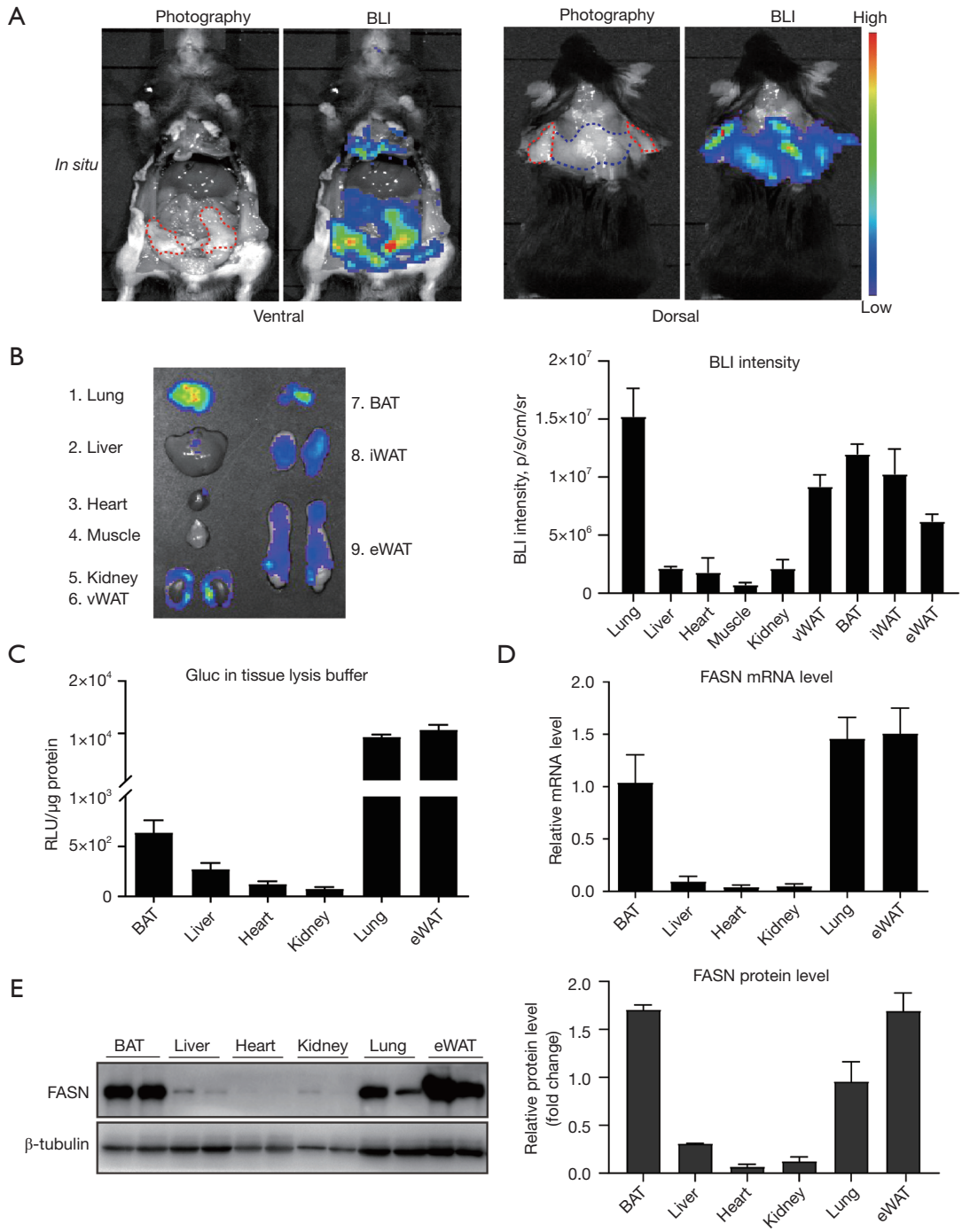

Figure 3 Organ-specific bioluminescence characteristics of FASN-2A-GLuc mice. (A) Bioluminescence emission of mouse abdominal cavity and scapula tissues *in situ*. The red dotted line points to WAT, and the blue dotted line points to BAT. (B) Ex vivo imaging (left) and quantification analysis (right) of bioluminescence in the freshly isolated lung, liver, heart, skeletal muscle, kidney, vWAT, BAT, iWAT, and eWAT samples. (C) Quantified GLuc activities in multiple tissue lysates. (D) FASN mRNA expression levels in multiple tissues from FASN-2A-GLuc mice. (E) Protein levels (left) and quantification (right) of FASN in multiple tissues. The values shown are expressed as mean ± SEMs (n=3). GLuc, Gaussia luciferase; WAT, white adipose tissue; vWAT, visceral WAT; BAT, brown adipose tissue; eWAT, epididymal WAT; iWAT, inguinal WAT; BLI, bioluminescence imaging; RLU, relative light units.

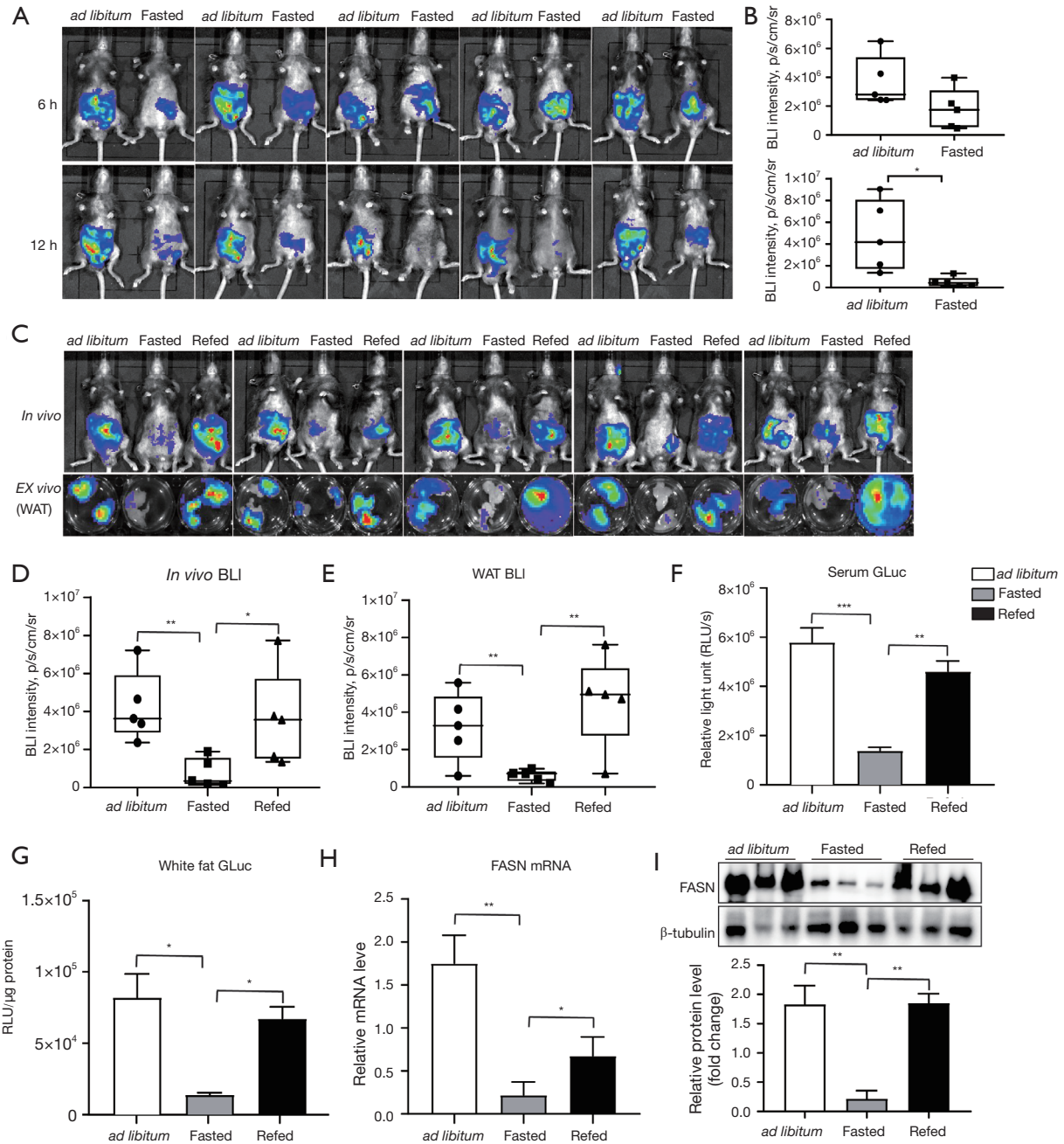

Figure 4 GLuc bioluminescence and FASN expression levels following *ad libitum* feeding, fasting, and refeeding. (A) *In vivo* BLI luminescence images of mice fasted for 6 h (top) or 12 h (bottom). (B) Quantification of the luminescence images shown in panel A. (C) Luminescence images of mice after *ad libitum* feeding, fasting for 24 h, and refeeding for 4 h after fasting, as determined *in vivo* and *ex vivo* (WAT). (D) Quantification of the luminescence images shown in panel C (top). (E) Quantification of the luminescence images shown in panel C (bottom). (F) GLuc luciferase activities in serum samples from FASN-2A-GLuc mice following *ad libitum* feeding, fasting, and refeeding. (G) GLuc activities in WAT protein lysates after *ad libitum* feeding, fasting, and refeeding. (H) FASN mRNA levels in WAT after ad libitum feeding, fasting, and refeeding. (I) Immunoblotting (top) and relative quantification (bottom) of FASN protein expression in WAT isolated from FASN-2A-GLuc mice after *ad libitum* feeding, fasting, and refeeding (n=5–6 mice/group). The data presented were analyzed by 1-way ANOVA and Student's *t* test. The graphs show mean values ± SEMs. *, P<0.05; **, P<0.01; ***, P<0.001. GLuc, Gaussia luciferase; BLI, bioluminescence imaging; WAT, white adipose tissue; ANOVA, analysis of variance; RLU, relative light units.

the bioluminescence signals were significantly lower in the fasted group than in the *ad libitum* group and fully recovered after refeeding, as determined by *in vivo* BLI (*Figure 4C*,*4D*) and *ex vivo* BLI in WAT (*Figure 4E*) and the liver (Figure S1A). We also detected GLuc activities in mouse serum (*Figure 4F*), WAT (*Figure 4G*), and liver lysates (Figure S1B) from the 3 groups, and the results were in accordance with the BLI results. Finally, we analyzed the mRNA and protein expression levels of FASN in WAT (*Figure 4H-4I*) and the liver (Figure S1C) under different dietary conditions. The results were consistent with the bioluminescence changes between the groups. These results demonstrated that our FASN-2A-GLuc mouse model accurately reflected dynamic changes in FASN levels in a visual and noninvasive manner.

Fatostatin inhibited DNL in high-carbohydrate water-induced FASN-2A-GLuc mice

Fatostatin is a synthetic chemical, formerly called 125B11, which was identified by screening for adipogenesis-blocking compounds in 3T3-L1 cells (25). Previous results showed that fatostatin could inhibit SREBPs, which are master transcriptional factors that regulate DNL (26). Previous findings also showed that fatostatin could reduce the weight of ob/ob mice and possesses high antitumor properties against various cancers (27,28). Using our reporter mouse model, we monitored the role of fatostatin in DNL induced by high glucose and fructose water. The results showed that bioluminescence decreased in WAT, BAT, and the lungs but not in the liver in the fatostatin group (*Figure 5A-5E*). The total bioluminescence tended to decrease in the fatostatin group (Figure S2). In addition, the changes in FASN mRNA expression levels in those tissues coincided with changes in bioluminescence intensities (*Figure 5F*). We also evaluated the energy metabolism characteristics of mice by performing metabolic cage experiments. In mice treated with fatostatin, the daily water intake (*Figure 5G*) and food intake (*Figure 5H*) decreased compared with those of the control group. We found that the RER increased significantly when mice were provided a high glucose and fructose solution. After treatment with fatostatin, the RER was lower than that in control mice, especially during the final 2 days, indicating that carbohydrate oxidation had decreased (*Figure 5I*). In summary, we found that fatostatin effectively inhibited DNL in multiple metabolic organs by *ex vivo* BLI. The FASN-2A-GLuc reporter mouse model provides a useful tool for screening preclinical drugs targeting the DNL pathway.

Discussion

Results of previous studies provided reliable evidence that blocking the DNL pathway may help prevent and treat obesity-related disorders (29-31). To facilitate progress in understanding these regulatory networks and screen for effective therapeutic agents, we generated a FASN-2A-Gluc reporter mouse model. This enabled us to dynamically and systemically monitor endogenous DNL *in vivo* and *ex vivo*.

Our FASN-2A-Gluc reporter mouse model enabled sensitive detection of bioluminescence signals for visualizing and quantifying DNL. We evaluated the global level of DNL activity with the reporter mice by performing *in vivo* BLI and detecting GLuc activity in mouse serum samples. By performing *ex vivo* BLI, we found that the bioluminescence approach accurately reported organ-specific FASN transcription following short-term starvation, long-term starvation, refeeding, or administration of fatostatin. Overall, our mouse model was not only easy to operate but had high sensitivity and accurate organ localization. Based on the complex role of DNL, it remains to be determined whether systemic or organ-specific inhibitors should be targeted, as their side effects and efficacies need to be considered. Thus, our reporter mouse model is highly suitable for drug evaluation at the systemic and organ-specific levels, which may become a trend in drug development that targets metabolic pathways. In addition, the model has advantages in studying tumor growth and metastasis related to DNL using *in vivo* BLI. However, there are still several limitations to this model. First, it is not applicable to study protein posttranslational modifications of FASN because the GLuc signal mainly reflects the transcriptional level of FASN. Secondly, this mouse model can elucidate potential targets' role in the DNL process by crossing with corresponding transgenic mice. However, cross-breeding 2 transgenic mice may take about 4 months, which is a relatively long time.

Currently, isotope labeling is the most commonly used method for monitoring metabolic flux. Hydrogen isotopes (^2H) of water have been used extensively to estimate DNL *in vivo*. ^2H_2O is administered orally or via intraperitoneal injection to achieve a target body water enrichment of 3–5%. The hepatic DNL can be assessed by measuring the appearance of ^2H in VLDL-palmitate-triglyceride using gas chromatography/mass spectrometry (32,33). This technique

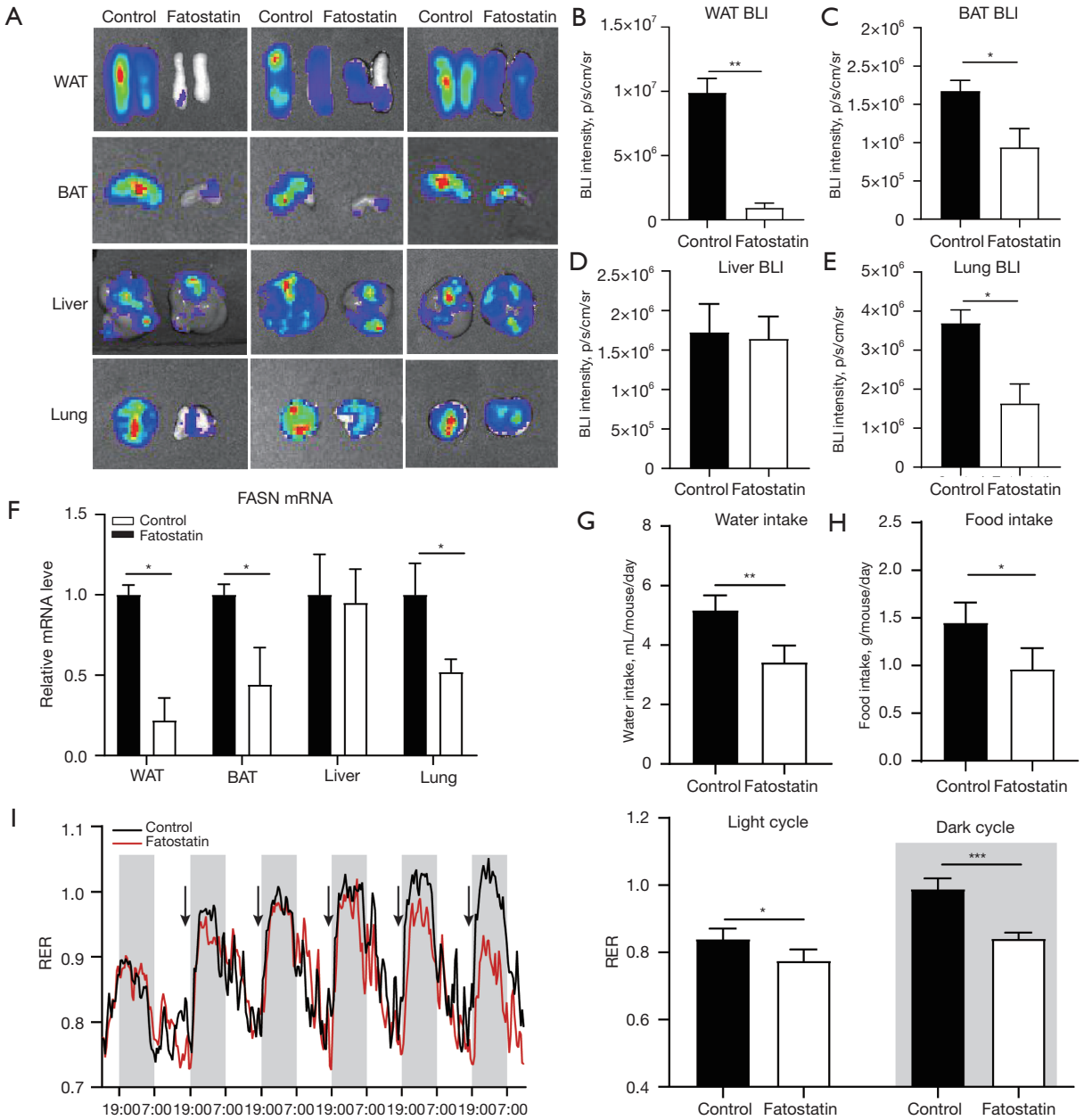

Figure 5 Fatostatin inhibited FASN expression in multiple tissues of FASN-2A-GLuc mice. (A) Luminescence images of mice after the fatostatin or control treatment, as determined by *ex vivo* BLI (WAT, BAT, liver, and lung samples). Quantification of luminescence signals in WAT (B), BAT (C), liver (D), and lung (E) samples. (F) mRNA expression levels of FASN in WAT, BAT, liver, and lung tissues in the fatostatin and control groups. (G) Quantification of water intake. (H) Quantification of food intake. (I) RER of mice after daily fatostatin or control treatment (left). Quantification of RER values during the last 2 days of treatment (right). The black arrows indicate the times of fatostatin treatment (n=5–6 mice/group). The data shown were analyzed with the Student's *t* test. The graphs show mean values ± SEMs. *, P<0.05; **, P<0.01; ***, P<0.001. GLuc, Gaussia luciferase; BLI, bioluminescence imaging; WAT, white adipose tissue; BAT, brown adipose tissue; RER, respiratory exchange ratio.

is applied to evaluate hepatic DNL in clinical patients. Compared with the isotope-labeling method, our mouse model is suitable for monitoring the dynamic changes of DNL systemically and organ-specifically in different conditions or treatments. Moreover, our mouse model has an advantage in the visual localization of DNL in metabolic diseases and related tumors.

By performing *ex vivo* BLI, this study found that fatostatin efficiently inhibited DNL in adipose tissues but not in the liver. This inhibition was related to the adipogenesis-blocking function of fatostatin (24). In previous studies, SREBP1 seemed to serve as a minor player during the DNL process in adipose tissues and to be important for the compensatory adaptations by SREBP2 (34,35). However, fatostatin can inhibit both SREBP1 and SREBP2, which can prevent compensatory effects. In addition, we found that fatostatin had an appetite-suppressant effect. In another study, fatostatin did not affect food intake in ob/ob mice. To some extent, this discrepancy may be related to a leptin deficiency in ob/ob mice, considering that leptin is an important hormone that controls feeding behavior (36). Thus, fatostatin is a potential therapeutic agent for obesity-related diseases based on its role in feeding behavior and DNL. It deserves further exploration in the context of the obesity mouse model.

Beyond metabolic disorders, many findings have demonstrated that DNL is upregulated during viral infections (which promotes membrane synthesis and viral replication), including in severe acute respiratory syndrome coronavirus 2 (SARS-CoV-2) (37). In one study, an FASN inhibitor blocked SARS-CoV-2 replication and reduced lung pathology (38). In our mouse model, we observed very high bioluminescence signals in the lungs, and we found that fatostatin also inhibited FASN expression in the lungs. Our FASN-2A-GLuc model may be a useful screening tool for identifying drugs or small-molecule compounds for COVID-19 therapies by targeting the DNL process.

This FASN-2A-GLuc reporter mouse model can be further used to elucidate the mechanisms of DNL regulation by employing it with other transgenic mice and administering different adeno-associated virus vectors. Furthermore, this model can be used to preclinically evaluate the efficacy of therapeutic agents targeting the DNL pathway or to potentially examine the side effects of some drugs on lipid metabolism.

Conclusions

In this study, we generated a real-time reporter mouse model to sensitively monitor and visualize endogenous FASN levels. This model can be used to study the dynamic regulation of DNL and screen for potential therapeutic agents that can treat obesity-related diseases.

Acknowledgments

Funding: This work was supported by the National Natural Science Foundation of China (Grant Nos. 81730016 and 81972761).

Footnote

Reporting Checklist: The authors have completed the ARRIVE reporting checklist. Available at https://atm.amegroups.com/article/view/10.21037/atm-22-1132/rc

Data Sharing Statement: Available at https://atm.amegroups.com/article/view/10.21037/atm-22-1132/dss

Conflicts of Interest: All authors have completed the ICMJE uniform disclosure form (available at https://atm.amegroups.com/article/view/10.21037/atm-22-1132/coif). The authors have no conflicts of interest to declare.

Ethical Statement: The authors are accountable for all aspects of the work in ensuring that questions related to the accuracy or integrity of any part of the work are appropriately investigated and resolved. All experimental procedures were performed under a project license (No. IACUC-20181204) by the Animal Welfare Ethics Committee of Air Force Medical University of PLA in China and were performed in accordance with the Guide for the Care and Use of Laboratory Animals, 8th edition.

References

1. Ameer F, Scandiuzzi L, Hasnain S, et al. De novo lipogenesis in health and disease. Metabolism 2014;63:895-902.
2. Shimano H, Sato R. SREBP-regulated lipid metabolism: convergent physiology - divergent pathophysiology. Nat Rev Endocrinol 2017;13:710-30.
3. Ortega-Prieto P, Postic C. Carbohydrate Sensing Through the Transcription Factor ChREBP. Front Genet 2019;10:472.
4. Yellaturu CR, Deng X, Cagen LM, et al. Insulin enhances post-translational processing of nascent SREBP-1c by promoting its phosphorylation and association with COPII vesicles. J Biol Chem 2009;284:7518-32.
5. Heidenreich S, Weber P, Stephanowitz H, et al. The glucose-sensing transcription factor ChREBP is targeted by proline hydroxylation. J Biol Chem 2020;295:17158-68.
6. Nuotio-Antar AM, Poungvarin N, Li M, et al. FABP4-Cre Mediated Expression of Constitutively Active ChREBP Protects Against Obesity, Fatty Liver, and Insulin Resistance. Endocrinology 2015;156:4020-32.
7. Nogalska A, Sucajtys-Szulc E, Swierczynski J. Leptin decreases lipogenic enzyme gene expression through modification of SREBP-1c gene expression in white adipose tissue of aging rats. Metabolism 2005;54:1041-7.
8. Imamura F, Fretts AM, Marklund M, et al. Fatty acids in the de novo lipogenesis pathway and incidence of type 2 diabetes: A pooled analysis of prospective cohort studies. PLoS Med 2020;17:e1003102.
9. Smith GI, Shankaran M, Yoshino M, et al. Insulin resistance drives hepatic de novo lipogenesis in nonalcoholic fatty liver disease. J Clin Invest 2020;130:1453-60.
10. Bian X, Liu R, Meng Y, et al. Lipid metabolism and cancer. J Exp Med 2021;218:e20201606.
11. Flannery C, Dufour S, Rabøl R, et al. Skeletal muscle insulin resistance promotes increased hepatic de novo lipogenesis, hyperlipidemia, and hepatic steatosis in the elderly. Diabetes 2012;61:2711-7.
12. Stanhope KL. Role of fructose-containing sugars in the epidemics of obesity and metabolic syndrome. Annu Rev Med 2012;63:329-43.
13. Brejchova K, Balas L, Paluchova V, et al. Understanding FAHFAs: From structure to metabolic regulation. Prog Lipid Res 2020;79:101053.
14. Zadra G, Ribeiro CF, Chetta P, et al. Inhibition of de novo lipogenesis targets androgen receptor signaling in castration-resistant prostate cancer. Proc Natl Acad Sci U S A 2019;116:631-40.
15. Zambito G, Chawda C, Mezzanotte L. Emerging tools for bioluminescence imaging. Curr Opin Chem Biol 2021;63:86-94.
16. Alsawaftah N, Farooq A, Dhou S, et al. Bioluminescence Imaging Applications in Cancer: A Comprehensive Review. IEEE Rev Biomed Eng 2021;14:307-26.
17. Ullah I, Prévost J, Ladinsky MS, et al. Live Imaging of SARS-CoV-2 Infection in Mice Reveals Neutralizing Antibodies Require Fc Function for Optimal Efficacy. Preprint. bioRxiv. 2021;2021.03.22.436337. doi:10.1101/2021.03.22.436337.
18. Shaikh FA, Kurtys E, Kubassova O, et al. Reporter gene imaging and its role in imaging-based drug development. Drug Discov Today 2020;25:582-92.
19. Wang H, Willershäuser M, Karlas A, et al. A dual Ucp1 reporter mouse model for imaging and quantitation of brown and brite fat recruitment. Mol Metab 2019;20:14-27.
20. Liu Y, Dentin R, Chen D, et al. A fasting inducible switch modulates gluconeogenesis via activator/coactivator exchange. Nature 2008;456:269-73.
21. Tannous BA. Gaussia luciferase reporter assay for monitoring biological processes in culture and in vivo. Nat Protoc 2009;4:582-91.
22. Schneider CA, Rasband WS, Eliceiri KW. NIH Image to ImageJ: 25 years of image analysis. Nat Methods 2012;9:671-5.
23. Szymczak-Workman AL, Vignali KM, Vignali DA. Design and construction of 2A peptide-linked multicistronic vectors. Cold Spring Harb Protoc 2012;2012:199-204.
24. Tannous BA, Teng J. Secreted blood reporters: insights and applications. Biotechnol Adv 2011;29:997-1003.
25. Choi Y, Kawazoe Y, Murakami K, et al. Identification of bioactive molecules by adipogenesis profiling of organic compounds. J Biol Chem 2003;278:7320-4.
26. Kamisuki S, Mao Q, Abu-Elheiga L, et al. A small molecule that blocks fat synthesis by inhibiting the activation of SREBP. Chem Biol 2009;16:882-92.
27. Talebi A, Dehairs J, Rambow F, et al. Sustained SREBP-1-dependent lipogenesis as a key mediator of resistance to BRAF-targeted therapy. Nat Commun 2018;9:2500.
28. Liu Y, Zhang N, Zhang H, et al. Fatostatin in Combination with Tamoxifen Induces Synergistic Inhibition in ER-Positive Breast Cancer. Drug Des Devel

Ther 2020;14:3535-45.
29. Batchuluun B, Pinkosky SL, Steinberg GR. Lipogenesis inhibitors: therapeutic opportunities and challenges. Nat Rev Drug Discov 2022;21:283-305.
30. Morrow MR, Batchuluun B, Wu J, et al. Inhibition of ATP-citrate lyase improves NASH, liver fibrosis, and dyslipidemia. Cell Metab 2022;34:919-936.e8.
31. Cohen CC, Li KW, Alazraki AL, et al. Dietary sugar restriction reduces hepatic de novo lipogenesis in adolescent boys with fatty liver disease. J Clin Invest 2021;131:e150996.
32. Fu X, Deja S, Fletcher JA, et al. Measurement of lipogenic flux by deuterium resolved mass spectrometry. Nat Commun 2021;12:3756.
33. Belew GD, Jones JG. De novo lipogenesis in non-alcoholic fatty liver disease: Quantification with stable isotope tracers. Eur J Clin Invest 2022;52:e13733.
34. Sekiya M, Yahagi N, Matsuzaka T, et al. SREBP-1-independent regulation of lipogenic gene expression in adipocytes. J Lipid Res 2007;48:1581-91.
35. Shimano H, Shimomura I, Hammer RE, et al. Elevated levels of SREBP-2 and cholesterol synthesis in livers of mice homozygous for a targeted disruption of the SREBP-1 gene. J Clin Invest 1997;100:2115-24.
36. Barrios-Correa AA, Estrada JA, Contreras I. Leptin Signaling in the Control of Metabolism and Appetite: Lessons from Animal Models. J Mol Neurosci 2018;66:390-402.
37. Koutsoudakis G, Romero-Brey I, Berger C, et al. Soraphen A: A broad-spectrum antiviral natural product with potent anti-hepatitis C virus activity. J Hepatol 2015;63:813-21.
38. Chu J, Xing C, Du Y, et al. Pharmacological inhibition of fatty acid synthesis blocks SARS-CoV-2 replication. Nat Metab 2021;3:1466-75.

Cite this article as: Li W, Zhang S, Fu X, Zhang J, Li R, Zhang H, An Q, Wang W, Tian Z, Shi C, Nie Y. Visualization and quantification of *de novo* lipogenesis using a *FASN-2A*-GLuc mouse model. Ann Transl Med 2022;10(18):958. doi: 10.21037/atm-22-1132

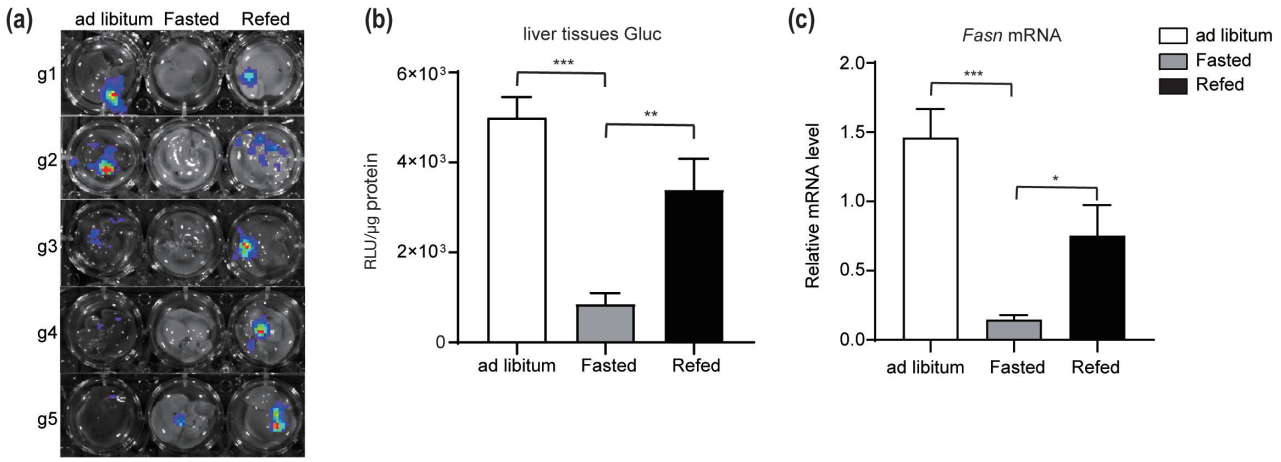

Figure S1 GLuc bioluminescence and FASN expression levels in liver tissues after *ad libitum* feeding, fasting, and refeeding. (A) Luminescence images of liver tissues after *ad libitum* feeding, fasting for 24 h, and refeeding for 4 h after fasting, as determined by *ex vivo* analysis. (B) GLuc activities in protein lysates of liver tissues after *ad libitum* feeding, fasting, and refeeding. (C) mRNA expression levels of FASN in liver tissues after *ad libitum* feeding, fasting, and refeeding (n=5 mice/group). The data shown were analyzed with a 1-way ANOVA and Student's *t* test. The graphs show mean values ± SEMs. *, P<0.05; **, P<0.01; ***, P<0.001. GLuc, Gaussia luciferase; ANOVA, analysis of variance; RLU, relative light units.

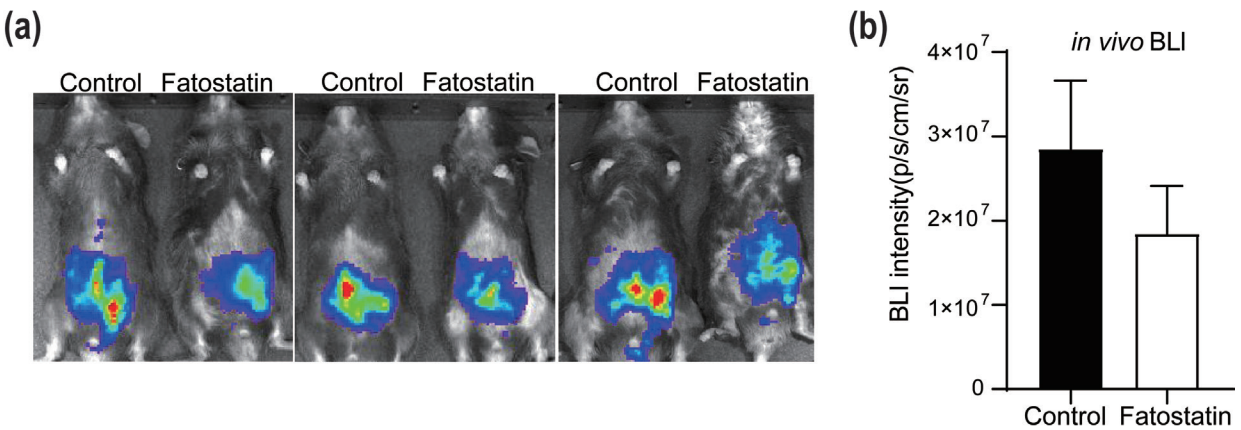

Figure S2 uminescence images of mice administered the fatostatin or control treatment, as obtained by *in vivo* BLI. (A) *In vivo* luminescence images. (B) Quantification of the luminescence images shown in (A). The data presented were analyzed with the Student's *t* test. The graphs show mean values ± SEMs. BLI, bioluminescence imaging.

https://dx.doi.org/10.21037/atm-22-1132